Accepted for publication in NDT&E, February 2016

Numerical Simulations of Ultrasonic Array Imaging of Highly Scattering Materials

Anton Van Pamel[1,2,a], Peter Huthwaite[1], Colin R. Brett[2], Michael J. S. Lowe[1]

[a] a.van-pamel11@imperial.ac.uk

Abstract

A Finite Element modelling framework is outlined that enables the investigation of ultrasonic array imaging within highly scattering, polycrystalline materials. Its utility is demonstrated by investigating the performance of arrays, within both single and multiple scattering media. By comparison to well-established single scattering models, it is demonstrated that FE modelling can provide new insights to study the stronger scattering regimes. In contrast to established single scattering results, Signal-to-Noise Ratio (SNR) no longer increases monotonically with respect to increasing aperture, which suggests that maximum apertures are not necessarily optimal. Furthermore, by measuring the SNR of the individual transmit receive combinations of the array, it is found that through separating the emitter and receiving source, it is possible to reduce the received backscatter.

Keywords: Ultrasonic Array Imaging, Grain Scattering.

[1] Imperial College London, Department of Mechanical Engineering , Exhibition Road, London, SW7 2AZ, UK
[2] E.ON Technologies (Ratcliffe) Ltd., Technology Centre, Nottingham, NG11 0EE, UK

1 Introduction

Ultrasonic arrays have enabled exciting possibilities for NDE in recent years. Not only have they been adopted for their ease of use, the wealth of spatial information [1] which can be acquired has enabled imaging capabilities which were previously inconceivable using monolithic transducers (see e.g. [2], [3]). Such advances have presented promising opportunities for progress but ultrasonic NDE still faces significant challenges: namely, it is fundamentally limited by the onset of scattering [4] once the probing wavelength becomes dimensionally similar to the microstructure of the propagation medium. For many materials, such as coarse grained polycrystalline metals [5], this occurs at typical inspection wavelengths. Consequent increases in attenuation, coherent noise, and possibly anisotropic effects, all contribute to a reduction in the Signal-to-(coherent)-Noise ratio (SNR), thereby limiting the range of materials which can be reliably inspected, ultrasonically.

Scattering within polycrystalline media has been studied in a great variety of contexts (see e.g. reviews [5], [6]) where an initial distinction can be made between single and multiple scattering regimes. Single scattering is a ‘weak’ scattering condition, generally accepted to be valid within the long-wavelength regime, where the polycrystalline material can be approximated by a random distribution of discrete scatterers and the contribution of each scatterer can be considered independently. The Independent Scattering Model (ISM) [7] is a well-respected implementation of this and has enabled notable progress [8] for the ultrasonic inspection of scattering materials. Single scattering assumptions however are known to become invalid for stronger scattering media once multiple scattering arises [9] .

Alternatively, numerical modelling currently presents opportunities to study these more challenging scattering regimes. Recent Finite Element (FE) models of elastodynamic wave propagation within polycrystalline materials [10]–[12] have been shown to capture the complex scattering physics [13], including multiple scattering [14], with high fidelity. These numerical methods can also be advantageous over experimental studies, as statistically significant studies are enabled by repeating multiple FE studies relatively inexpensively, and with complete knowledge and control of the parameters.

Such advantages present FE as an ideal tool to provide a quantitative understanding and answer the remaining questions (see e.g. [15]) to determine the optimal array parameters to for instance maximise imaging SNR and by association the possibility of a successful detection. The latter can involve a multitude of parameters to optimise, associated to either hardware (e.g. the aperture size) or software (e.g. the imaging algorithm). Here we pursue an initial interest in the array configuration, including its number of array elements, which defines the aperture angle and the element layout, and therefore we constrain software parameters such as the imaging algorithm.

Within the field of ultrasonic array imaging, there has been a recent surge of advanced imaging algorithms (see e.g.[2], [3] and reviews [16], [17]) which have shown impressive progress. Still, it has proven challenging to suppress coherent noise [16], [17] and thereby increase imaging performance beyond that provided by standard sum-and-delay beamforming. Consequently, the currently most popular algorithm, the Total Focusing Method (TFM)[18] , for the time being, remains the benchmark, offering both high performance as well as relative simplicity. Thus this article will rely on TFM for its investigations and illustrations; it is expected that the findings will be equally relevant for other imaging algorithms.

This article outlines a FE modelling framework, an extension to the basis reported in [10]–[14], that enables the investigation of ultrasonic array imaging of highly scattering, polycrystalline materials. It details modelling devices which allow the isolation of different physical phenomena (e.g. element directivity, beam spreading, attenuation, backscatter) and therefore enables new and useful insights into the effects of scattering, particularly without relying on a single scattering assumption. The methodology is applied to a relatively simple but also general case such that it both illustrates and investigates the fundamentals of array performance. The approach is now also ready for a wide variety of simulations where it can be useful in future evaluations of performance: for instance to determine the optimal configuration for a more practical inspection, quantify the smallest detectable defect, or assess new data processing algorithms such as new candidate array imaging algorithms.

The subsequent sections are organised as follows. Section 2 outlines the FE methodology starting with the description of a polycrystalline medium and later the ultrasonic array models. Before considering polycrystalline scattering media, Section 3 uses established theory to study array performance within a single scattering environment. These results enable comparisons with Section 4 which repeats the same procedure but considers stronger, multiple scattering by introducing polycrystalline material properties. Section 5 then compares the results obtained from both previous sections. Before setting out with these studies, we present the currently established theory for determining detection performance of an array imaging a noisy medium, under single scattering assumptions.

1.1 Established Single Scattering Theory

In many circumstances of NDE, such as the inspection of acoustically transparent materials, detection performance is predominantly defined by random noise such as electrical noise. Once scattering occurs, coherent noise manifests and typically becomes the limiting factor. Assuming that random noise has been eliminated by, for example, temporal averaging, SNR will hereon refer to the Signal-to-(coherent)-Noise Ratio.

Single scattering models, such as the aforementioned ISM [19], [20], determined that SNR is inversely proportional to the ultrasonic pulse volume for monolithic transducers. This led to the adoption of focused transducers to improve sensitivity of industrial inspections of scattering materials. More recently, Wilcox [4] (and others e.g. [21]) found similar results for arrays by showing SNR to depend on the Point-Spread Function (PSF) of an array (see Equation 1).

$$SNR(\boldsymbol{r}) = \frac{q}{\mu}\frac{|P(\boldsymbol{r},\boldsymbol{r})|}{\sqrt{\int |P(\boldsymbol{r},\boldsymbol{r}')|^2 dr'}} \tag{1}$$

Here μ is the backscatter coefficient, derived for polycrystalline materials by Rose [22] and q is the scattering potential of the imaging target. Outside these two parameters, the remainder of Equation 1 is defined by two Point Spread Functions, e.g. P(**r**,**r'**) is the image response at **r** of an idealised single point scatterer located at ***r'***. Thus the remaining fraction is solely determined by the imaging system and is equivalent to the reciprocal of the square root of the normalized PSF area [4], σ. For our purposes of finding an optimum, only relative SNR is of interest, and hence in the studies presented here we can disregard the two parameters μ and q [21] and redefine a relative SNR, denoted by $\overline{SNR_p}$, where pk denotes peak.

$$\overline{SNR_p}(\boldsymbol{r}) = \frac{|P(\boldsymbol{r},\boldsymbol{r})|_{pk}}{\sqrt{\int |P(\boldsymbol{r},\boldsymbol{r}')|^2 dr'}} \tag{2}$$

The relation between SNR and the PSF has several interesting connotations. It firstly implies the monotonic increase of SNR which improves as the PSF is reduced. SNR is thus maximised when using the largest possible aperture [23]. The PSF area, σ, is a widely used metric and can be quantified in various ways (see e.g. [18]), the approach adopted here is to calculate the area of the PSF which encompasses half its peak, and subsequently normalise it against the centre-wavelength squared, denoted by $\overline{\sigma}$.

The PSF comprises the imaging system and can thus be controlled by optimising the array and the imaging algorithm; as previously mentioned, we will focus on the former using a specific choice of imaging algorithm.

2 Method: Finite Element Simulation of Highly Scattering Materials

Here we discuss how to incorporate polycrystalline material properties into an FE model, followed by its extension into our model of an ultrasonic array, which consists of a noise and a signal model.

2.1 Polycrystalline Material Model

Whereas time-domain explicit FE modelling of wave propagation within isotropic media is well established [24], incorporating a polycrystalline microstructure is a relatively new addition [10]–[12] which is becoming increasingly popular [13], [14]. The methodology, as used here, relies on a Voronoi approach which is widely used in other fields of research such as that of material science (see e.g. [25]) to generate random tessellations which are representative of polycrystalline morphologies. The main obstacle to its adoption for the study of dynamic wave propagation has been its computational cost which is significantly higher than for conventional wave propagation modelling [24] due to a more demanding mesh sampling criterion, defined by the grain size. The simulation package used here is Pogo [26] and the mesh comprises a structured grid of triangular elements, sampled such that the length of the element edge is finer than at least one tenth of the average grain size d to meet the criteria for convergence.

Given the already large computational cost, the relatively large dimensions necessary for our studies, and the interest in performing multiple analyses in order to pursue a range of studies, the models discussed here are limited to a 2D domain. This simplification introduces certain model limitations (discussed in more detail in [13]): the scattering mechanism is reduced to a third order frequency dependence in the Rayleigh regime as shown in [13], [27], and it is not obvious how to relate the spatially incoherent fields, namely the grain noise, perceived by a 2D transducer to that of a 3D one. It is expected that 2D models overestimate the absolute level of noise as there is less spatial averaging which occurs across the length of the transducer, as opposed to an equivalent area in 3D. Despite this lack of absolute accuracy, the relative accuracy is expected to be good, as the overall frequency dependent scattering behaviour has been shown to correlate well to established theory [13]. This is deemed sufficient as we are primarily interested in examining trends and principles rather than absolute performance metrics. Moreover, the principles discussed in this paper will apply equally well in 3D, and since 3D representation has been shown to be possible [13], it will only be a matter of deploying these methods in 3D once this becomes computationally feasible.

2.2 Array Model

The layout for the general ultrasonic array model used hereon is depicted in Figure 1a. The model typically simulates N=128 element arrays which are fully sampled, such that the array pitch and width both measure half a wavelength at the centre-frequency (hereon referred to as a centre-wavelength). The array data acquisition adopts a Full-Matrix-Capture (FMC) [18] approach which involves sequentially exciting all N array elements, and for each excitation, calculating the response also on all N array elements. The excitation at the i^{th} element of the array is simulated by applying a force load which is perpendicular to the surface (producing a longitudinal wave but also spurious shear waves), to all the nodes which correspond to the footprint of the i^{th} array element. In reception, the nodal displacements of all the nodes belonging to the j^{th} array element are averaged, again taking the component of displacement in the direction normal to the surface. Varying both j and i from 1 to N, this populates an FMC matrix, H, of dimensions $N \times N \times t$ where t corresponds to the number of time samples.

2.2.1 Noise Model

Before the introduction of any imaging target within the model, this procedure yields an array response matrix, H_N, which pertains solely to the grain noise (and reflections from the structural boundaries). This can be thought of as an artificial baseline measurement, as is commonly referred to in Structural Health Monitoring [28]. This is useful for separately analysing the signal and noise data which enables monitoring the true SNR. This is a valuable tool in general, as investigations are often limited to measure signals which contain noise, thereby constrained to solely measuring positive SNRs [17] which offer a limited utility as a performance metric. There are several ways to circumvent this, one being subtraction [29], and another which is outlined in the proceeding sub-section.

2.2.2 Signal Model: True Point Scatterer

To obtain the previously defined PSF, we desire an ideal, omnidirectional scatterer - here referred to as a true point scatterer (TPS). A widely accepted practice is to use voids or disconnections within an FE mesh to simulate defects and scatterers. The obvious procedure to create a single point scatterer then would be to constrain or disconnect a single node. However, for scattering within elastic materials this does not produce a true omnidirectional scatterer; instead of the desired isotropic scattering, the scattering amplitude of the longitudinal wave varies with angle, dropping to null as the difference between the incident and scattered wave approaches 90°.

This is circumvented here by exploiting reciprocity which allows us to reverse the sender and receiver. Instead of insonifying the domain using the array, and looking for scattering back from the defect, the defect is used to insonify the domain, and the projected wave field is received by the array to produce a Nxt matrix h_s. The principle of reciprocity can thereafter be used to complete the send-receive signals of the array FMC. Namely, the full FMC, corresponding to the signal model, H_S, is obtained by convolution of the $N\times t$ vector of received signals, h_s, with its transpose, to obtain the $N\times N\times t$ matrix.

This approach enables controlling the scattering characteristics of the defect, as previously mentioned, one which exhibits uniform omnidirectional scattering is desired. This requires the excitation of a circular wavefront outgoing from the point scatterer, which is achieved here by radially exciting six neighbouring nodes of a structured mesh in a hexagonal arrangement (see Figure 1b). The resultant wave field from such a point source is illustrated in Figure 2, within (a) an isotropic and (b) polycrystalline medium.

One noteworthy consequence of this approach is that the scattering potential of our imaging target (denoted by q in Equation 1) is arbitrarily defined by the excitation amplitude defined in the FE simulation. Moreover, we cannot calculate an effective incident amplitude for the circular wave, as a singularity exists at the centre where the radius equals zero and the theoretical incident amplitude tends to infinity. In our case however, as discussed in Section 1.1, we are only interested in a relative SNR to find an optimum, and hence to clarify this, we shall distinguish from the SNR by the term $\overline{SNR}$ to denote a relative quantity.

3 Results I: Simulation of Single Scattering Media

The single scattering theory [4] outlined in Section 1.1 is now used to validate a Finite Element model of an array operating within a single scattering medium, here modelled by a random distribution of point scatterers within an isotropic material. By adopting a single scattering assumption, we can solve the PSF for each scatterer independently [4], [16]. Furthermore, when considering both the noise scatterers and the imaging target as omnidirectional scatterers, the solution of one PSF provides that for all others, be it grain noise or target [4], [16]. This approach purposefully neglects any multiple scattering effects, which serves as a benchmark for comparisons when the polycrystalline microstructure is introduced later on (see Section 4).

The model defines a fully sampled N=128 element array, generating a 3-cycle tone-burst longitudinal wave with a 2MHz centre-frequency in contact with an isotropic elastic material. The medium is arbitrarily defined by a longitudinal wave speed of 6123m/s (E=230GPa, ν=0.3, ρ= 8200kg/m^3). Three defect scenarios are simulated to calculate H_s for a TPS defined by the procedure in Section 2.2.2, and introduced respectively at a 25mm, 50mm, and 75mm depth within the material.

3.1 True Point Scatterer

The behaviour of our model TPS within an isotropic material is validated by calculating apparent scattering matrices [30], [31] from H_s. An amplitude scattering matrix procedure follows [31], however, unlike classical scattering matrices, our setup comprises a linear array with a limited view to sample the wave field, rather than a circumferential full view configuration. Adopting the notation of an analytical signal [32] the amplitude matrix used here plots the instantaneous amplitude $A(t_0)$, where t_0 corresponds to the arrival time of the signal, as a function of incident θ_i and scattered θ_s angle (defined in Figure 1a), to produce a 2D matrix $A(\theta_{i,},\theta_s)$. A phase matrix is also calculated which follows the same syntax but instead of amplitude, calculates the instantaneous phase $\phi(t_0)$ to obtain $\phi(\theta_i,\theta_s)$. An example of how to calculate both instantaneous amplitude and instantaneous phase can be found in [33].

As can be seen from the amplitude scattering matrix in Figure 3a, the TPS defect exhibits omnidirectional scattering behaviour, as intended. Due to the absence of noise and attenuation in this case, the only drop in scattering amplitude occurs due to longer propagation distances and large receiver angles. The longer propagation distances will cause the wave amplitude to decrease due to beam spreading effects, and a loss in element sensitivity occurs at large angles as the array elements exhibit a directional sensitivity, which reduces as the incident wave moves away from the normal. The rhomboidal features manifest at larger angles are due to the linear array configuration where the propagation distance is not constant with total aperture angle (propagation distance increases non-linearly with angle). Figure 3b confirms the expected absence of aberrations in the phase matrix for the isotropic case, where the extremely small changes observed are numerically insignificant.

3.2 Point Spread Function

The PSF for a TPS within an isotropic medium is shown in Figure 4a. Characteristic low-intensity side lobes can be identified and the slightly non-circular appearance of the main lobe is due to array being linear rather than having a circumferential full-view configuration. The normalised PSF area ($\overline{\sigma}$) is quantified as a function of the half aperture angle, denoted by θ_p and calculated by the halved sum of θ_i *and* θ_s. As previously defined, our definition of PSF calculates the area which encloses the PSF within -6dB from its peak and is normalised against the centre-wavelength squared.

Figure 5a plots the resultant *PSF* area ($\overline{\sigma}$) as a function of half aperture angle θ_p, for three TPS at various depths. As can be seen the PSF decreases monotonically, where focusing benefits progressively lessen at high aperture angle as is dictated by the asymptotical diffraction limit [4].

3.3 Predicted Signal-to-Noise Ratio

The previously obtained PSF now allows the prediction of a relative SNR in a single scattering environment, $\overline{SNR_P}$, as defined in Equation 2. Figure 5b shows $\overline{SNR_P}$ versus half aperture angle θ_p and predicts a monotonically increasing SNR, independent of defect depth. These results agree with the experimental and model findings of Wilcox [4], thereby validating our single scattering model. Now we investigate the effects of multiple scattering by repeating the same simulation but with the introduction of polycrystalline material properties.

4 Results II: Simulation of Multiple Scattering Media

The procedure outlined in Section 3 is now repeated for a polycrystalline medium which introduces inherent scattering and thus no longer relies on a single scattering assumption. Using the same layout depicted in Figure 1a, with a 2MHz 3-cycle tone-burst, exciting longitudinal waves from a *N*=128 element array, images are acquired of targets buried at depths of 25mm, 50mm, and 75mm. The medium comprises cubic Inconel 600, non-textured and monophasic, defined by the single elastic stiffness constants taken from [14] (see Table 1). The grain morphology consists of equiaxed grains with their mean size set at 500μm (and a standard deviation of 70 μm), which places the scattering behaviour at centre-wavelength, in between the Rayleigh and stochastic scattering regimes. Although we are not aware of a formal definition for its onset, for the material considered here which exhibits a relatively high anisotropy (anisotropic ratio, A=2.8), it is believed that multiple scattering occurs within the stochastic regime which begins for kd values of unity, where k is the wavenumber and d is the mean grain size. Eight independent models are run, each with the same mean grain properties but different realisations of a random morphologies and orientations. This provides us with a basis, albeit with a modest number of samples, to consider statistical variations.

In contrast to the single scattering results in Section 3, where the PSF provided solutions for both the noise and signal model, separate simulations are now required to obtain the noise data H_N and H_s: the data from a TPS.

4.1 Aberrated True Point Scatterer

Similarly to Section 3.1, we establish the behaviour of a TPS, in this instance however by considering propagation within a polycrystalline medium. In comparison to the isotropic medium considered in Section 3, which incorporated beam spreading and element directivity, our signal model, H_s, now includes additional physics such as the scattering induced attenuation, dispersion, and phase aberrations.

The scattering amplitude and phase matrices (see Section 3.1 for methodology) for a TPS at 25mm depth, are shown in Figure 6 for one random realisation of a polycrystalline material. When compared to the isotropic case in Figure 3 it can be seen that the amplitude fluctuates, but in general depicts a similar picture to that of the isotropic case where the highest amplitudes occur at (0°,0°) angles. In terms of phase however, whereas Figure 3b showed no variations for the isotropic case, significant phase aberrations can be seen of up to 1π radians. This observation is further illustrated in the earlier Figure 2b, where aberrations can be seen to occur along the circular wavefront. These aberrations in the phase matrix also appear to reveal some regularity, namely there seems to be some symmetry. This is possibly due to dispersion which has a different effect for longer propagation paths. However, even in a non-dispersive medium there will be some regularity to this matrix, since, as illustrated by our reciprocity method to calculate H_s, there are only N unique values corresponding to those of h_s. The phase matrix has illustrated some of the detrimental effects which can be expected to significantly hinder focusing ability of the array, which is quantified next by calculating the PSF.

4.2 Aberrated Point Spread Function

Figure 4b shows an aberrated PSF for a TPS within a polycrystalline material where perturbations have now arisen when comparing to Figure 4a. The normalised PSF area is calculated similarly to the procedure adopted in Section 3.2, but repeated for eight realisations of a random polycrystalline material to consider statistical variation. The eight PSF areas are then averaged and their standard deviation is also recorded.

Figure 7a plots the mean normalised PSF area ($\overline{\sigma}$) and its standard deviation bars, versus half aperture angle, θ_p, for the three TPS cases. Comparison with Figure 5a reveals that the polycrystalline material has induced several changes. Firstly, it can be seen that the absolute focus has worsened, indicating a PSF which is larger relative to the previous case. This indicates that even before considering the effects of coherent noise, which probably presents further hindrance to image quality, the focus (which is related to SNR) has already been harmed. Furthermore, although PSF area remains a monotonic function with respect to aperture angle, it has become also a function of depth. Several physical effects can contribute to this effect, such as the scattering induced attenuation which removes more high frequency information for the longer propagation paths and thereby reduces focusing.

Similarly to the previous section, the PSF enables a prediction of SNR, as defined in Equation 2. Figure 7b plots the resulting $\overline{SNR_P}$ versus half aperture angle θ_p and as can be seen, depicts a similar picture to that of Figure 7a. It must be noted that this prediction is based on single scattering assumptions, and as previously mentioned, is no longer valid within a multiple scattering regime. Instead however, since both signal and noise data are available, the SNR can be measured.

4.3 Measured Signal-to-Noise Ratio

Following the procedure for a noise model outlined in Section 2, H_N is calculated by using the same eight material realisations mentioned earlier, however removing the defect and sequentially exciting the array to obtain a baseline FMC. This produces an array image as shown in Figure 4c. From such an array image, similar to [16], we can calculate the Root-Mean-Square (RMS) of the pixel intensities at an image area of interest, to obtain a measure of the noise.

This noise data becomes useful when combined with the previously obtained H_s, as it enables a calculation of the $\overline{SNR_m}$, in this case performed as a function of aperture θ_p. The signal intensity is calculated from the peak pixel intensity (pk) within the array image I_s (the PSF in this case shown in Figure 4b). The noise area considered forms a box around the hypothetical defect which extends 10mm beyond the defect in the negative and positive, lateral and axial directions of the noise image I_N (see Figure 4c). SNR is subsequently calculated as shown in Equation 3 where $\langle\ \rangle_{xy}$ denotes the mean across both x and y. To distinguish from the previous SNR, we shall label this the $\overline{SNR_m}$.

$$\overline{SNR_m}\,(\theta p) = \frac{|I_s(x, y, \theta p)|_{pk}}{\sqrt{\langle I_N(x, y, \theta p)^2 \rangle_{xy}}} \tag{3}$$

4.3.1 Aperture

Figure 8 plots the mean image $\overline{SNR_m}$ and the standard deviation bars for 8 different random realisations of materials, for the three TPS cases as a function of half aperture angle. As was previously predicted by the aberrated PSF results, SNR becomes a function of depth. Contrastingly however, it can be seen that SNR no longer behaves monotonically with respect to aperture angle; beyond an initial increase with aperture, it decreases for the widest aperture angles. Hence unlike the findings from Section 3, this suggests for the strong scattering regime considered here, that the largest array aperture does not always optimise image SNR. This reaffirms that within the highly scattering regimes considered here, single scattering approximation no longer apply and new methods are required, such as those shown here.

4.3.2 SNR Matrix

Taking the analysis one step further, and similar to the previously mentioned scattering matrix calculations (see Section 3.1), equivalent noise and SNR matrices are calculated. The noise matrix is computed using the amplitude matrix procedure but instead of calculating the instantaneous amplitude at t_0, an average noise level is calculated, defined by the RMS value of a 1μs time-window surrounding t_0. The SNR matrix is then obtained by the division of the signal and noise scattering matrices, similar to Equation 3. Although it may be more intuitive to plot the noise matrix against the received and emitted array element index, we will maintain the scattered and incident angle labels for consistency with the SNR matrix.

Figure 9 plots the (a) mean noise and (b) mean $\overline{SNR_m}$ as a function of received and scattered angle, θ_i, and θ_s, averaged for eight realisations of the 25mm depth TPS. Several observations can be made. Firstly, high intensity noise and low SNR can be found along the leading diagonal of Figs 9a and 9b respectively, which corresponds to the pulse-echo elements exhibiting the worst SNR. This is a coherent multiple scattering effect (see e.g. [34]) previously known to manifest also in FE simulations of elastic wave scattering [14]. Due to reciprocity, a multiple scattering source-receiver path illuminates in both the direct and reciprocal directions, hence doubling the intensity of the received noise. This explains why in practice twin-crystal probes have been observed to perform better than pulse-echo inspections relying on single probes to inspect highly scattering materials.

Another interesting feature is the presence of a noisy region which comprises a band adjacent and roughly parallel to the leading diagonal in Figure 9a. Within the band we can make several observations. Firstly by assessing the change in noise along the leading diagonal and those adjacent but also parallel to it, we can see that the measured noise amplitude decays very slowly if at all, which shows that backscatter is a weak function of depth in this case (as the angle between receiving and transmitted array element is constant along these lines). Contrarily, the noise seems to decay much quicker in the direction which is normal to the leading diagonal which suggests a much stronger dependence on angle. In addition, before reducing to lower levels of backscatter, towards the edge of the band there is a significant rise in backscatter which is shown by the quarter-circle bands (labelled R in Figure 9a) and correspond to the Rayleigh wave (i.e. the Rayleigh wave in these cases arrived at previously defined t_0). Thus the high noise region contained within this band (defined for one side of the matrix by a dashed line in Figure 9a), hereby termed the backscatter envelope, can be broadly defined by the time-window corresponding to the arrival from transmitter to receiver of the Rayleigh wave.

The implication of the backscatter envelope is that it presents an opportunity to operate outside it. Namely, using large pitch-catch angles allows a longitudinal wave to arrive at the receiver before the majority of backscatter has arrived. This implies that pitch-catch configurations, using for example two arrays to separate the emitter and receiver, can be advantageous. At large aperture angles, it is possible that electrical noise sources become more significant as the received signal amplitudes, depending on the defect, can be significantly reduced. Such incoherent noise problems are much easier to overcome than coherent ones however, and hence in certain scenarios, it is possible that operating outside the backscatter envelope may provide benefits.

5 Discussion: Spatial Averaging Theory

The findings from Section 3 and 4 can be combined to compare the prediction of $\overline{SNR_p}$ using the aberrated PSF (results from Section 4.2 and Equation 2) to that obtained from the full signal and noise measurements $\overline{SNR_m}$ (Section 4.3 and Equation 3). In addition however, a simplifying argument is proposed here, namely one which assumes that within highly scattering environments, the noise, albeit temporally coherent, is entirely uncorrelated between the different array elements (i.e. spatially incoherent). This would enable modelling of the noise by an averaging law which is simply the reciprocal of square-root n, where n represents the number of spatially independent time-traces used. Although the FMC holds N^2 time-traces, $n=N(1+N)/2$ due to reciprocity. Namely, in the absence of temporally random noise (e.g. electrical) only the half of the FMC (known as Half Matrix Capture (HMC)) holds unique information, as reciprocity dictates that a sender and receiver combination can be reversed and the received wave field remains identical. This defines a new SNR based on averaging theory, $\overline{SNR_a}$ defined in Equation 4.

$$\overline{SNR_a}\,(N) = \frac{|I_s(x, y, \theta p)|_{pk}}{\sqrt{N(1+N)/2}} \tag{4}$$

As an initial verification, Figure 10 plots the RMS image noise amplitude against the averaging law. It shows good overall matching; the closest match occurring for the noise which stems deepest within the material (i.e. 75mm). Interestingly, this suggests that the grain noise is largely uncorrelated between array elements in the highly scattering regime simulated here.

5.1 Comparison of Multiple Scattering Results to Single Scattering Theory

The SNR comparisons are shown in Figure 11a-c for the three TPS. The $\overline{SNR_m}$ is shown with error bars, against both theoretical predictions, $\overline{SNR_p}$ and the averaging law $\overline{SNR_a}$. The correlations for both theories are qualitatively good in (b) and (c), and less so for case (a). In general, the averaging approximation is the better of the two as the limitation of the single scattering theory is that it only predicts monotonic SNR functions. Within the materials simulated, when multiple scattering arises, this is shown not to be the case, and hence the degradation of signal information through attenuation, phase aberration, and possibly dispersive effects are detrimental to the performance of the array.

When using a single array, this notion suggests that for a given array element budget, it is preferable to spend it on a 2D configuration (to obtain either a spatially compounded 2D or 3D image), i.e. rather than arrange the elements along a line, to extend them into a grid. A similar amount of spatial averaging will occur but more importantly, the signal information captured by the array will maintain a higher quality (amplitude).

6 Conclusions

This article has described a FE modelling framework to simulate ultrasonic arrays imaging within highly scattering, polycrystalline materials. Its utility is demonstrated by investigating the performance of array imaging, which is fundamentally limited by the onset of scattering noise. By comparison of multiple scattering simulations results to those of well-established single scattering models, it is found that FE modelling can provide interesting and new insights to study the stronger scattering regimes. It must be noted that the simulations were confined to a 2D domain, which doesn’t fully capture the physics of 3D scattering.

The numerical simulations found that within highly scattering environments, the maximum aperture does not necessarily maximise the SNR, which suggests that 2D arrays should offer improved performance over linear arrays. By demonstrating the existence of a backscatter envelope, it is also shown that in certain inspection scenarios, significant advantages can be derived from separating the emitting and receiving transducer. Lastly, it was found that treating the noise as spatially incoherent between the different array elements makes as a good approximation as a noise model in this strong scattering case.

7 Acknowledgements

This work has been supported by the UK Research Centre in NDE and the Engineering and Physical Sciences Research Council grant EP/I017704/1.

8 References

[1] P. D. Wilcox, "Ultrasonic arrays in NDE: Beyond the B-scan," *Rev. Prog. Quant. NDE (AIP Conf. Proc. vol 1511)*, pp. 33–50, Jan. 2013.

[2] A. Aubry and A. Derode, "Detection and imaging in a random medium: A matrix method to overcome multiple scattering," *J. Appl. Phys.*, vol. 106, no. 044903, 2009.

[3] F. Simonetti, "Multiple scattering: The key to unravel the subwavelength world from the far- field pattern of a scattered wave," *Phys. Rev. E*, vol. 73, no. 3, pp. 1–13, 2006.

[4] P. D. Wilcox, "Array imaging of noisy materials," *Rev. Prog. Quant. NDE (AIP Conf. Proc. vol 1335)*, pp. 890–897, 2011.

[5] E. P. Papadakis, "Scattering in Polycrystalline Media," in *Ultrasonics: Methods in Experimental Physics*, P. D. Edmonds, Ed. New York: Academic Press, 1981, pp. 237–298.

[6] R. B. Thompson, F. J. Margetan, P. Haldipur, L. Yu, A. Li, P. Panetta, and H. Wasan, "Scattering of elastic waves in simple and complex polycrystals," *Wave Motion*, vol. 45, no. 5, pp. 655–674, 2008.

[7] F. J. Margetan, R. B. Thompson, and I. Yalda-Mooshabad, "Backscattered microstructural noise in ultrasonic toneburst inspections," *J. Nondestruct. Eval.*, vol. 13, no. 3, pp. 111–136, Sep. 1994.

[8] F. J. Margetan, M. Gigliotti, L. Brashe, and W. Leach, "Fundamental studies: inspection properties for engine titanium alloys," in *FAA Report DOT/FAA/AR-02/114*, 2002.

[9] A. Aubry and A. Derode, "Random matrix theory applied to acoustic backscattering and imaging in complex media," *Phys. Rev. Lett.*, vol. 102, no. 8, p. 84301, 2009.

[10] G. Ghoshal and J. a. Turner, "Numerical model of longitudinal wave scattering in polycrystals," *IEEE Trans. Ultrason. Ferroelect. Freq. Control*, vol. 56, no. 7, pp. 1419–1428, 2009.

[11] B. Chassignole, V. Duwig, M.-A. Ploix, P. Guy, and R. El Guerjouma, "Modelling the attenuation in the ATHENA finite elements code for the ultrasonic testing of austenitic stainless steel welds.," *Ultrasonics*, vol. 49, no. 8, pp. 653–8, 2009.

[12] N. Feuilly, O. Dupond, B. Chassignole, J. Moysan, and G. Corneloup, "Relation between ultrasonic backscattering and microstructure for polycrystalline materials," *Rev. Prog. Quant. NDE (AIP Conf. Proc.*

vol 1096), pp. 1216–1223, 2009.

[13] A. Van Pamel, P. Huthwaite, C. R. Brett, and M. J. S. Lowe, "Finite Element Modelling of Elastic Wave Scattering in Polycrystalline Media," *J. Acoust. Soc. Am.*, vol. 138, no. 4, p. 2326, 2015.

[14] S. Shahjahan, F. Rupin, A. Aubry, B. Chassignole, T. Fouquet, and A. Derode, "Comparison between experimental and 2-D numerical studies of multiple scattering in Inconel600 by means of array probes.," *Ultrasonics*, vol. 54, no. 1, pp. 358–67, 2014.

[15] P. D. Wilcox, "Optimization of array element pitch for NDE applications," in *AIP Conference Proceedings*, 2015, vol. 1650, no. 1, pp. 952–961.

[16] J. Zhang, B. W. Drinkwater, and P. D. Wilcox, "Comparison of ultrasonic array imaging algorithms for nondestructive evaluation," *IEEE Trans. Ultrason. Ferroelect. Freq. Control*, vol. 60, no. 8, pp. 1732–1745, Aug. 2013.

[17] A. Van Pamel, C. Brett, and M. Lowe, "A methodology for evaluating detection performance of ultrasonic array imaging algorithms for coarse-grained materials," *IEEE Trans. Ultrason. Ferroelect. Freq. Control*, vol. 61, no. 12, pp. 2042–2053, 2014.

[18] C. Holmes, B. W. Drinkwater, and P. D. Wilcox, "Post-processing of the full matrix of ultrasonic transmit – receive array data for non-destructive evaluation," *NDT E Int.*, vol. 38, pp. 701–711, 2005.

[19] F. J. Margetan, R. B. Thompson, and I. Yalda-Mooshabad, "Modeling Ultrasonic Microstructural Noise in Titanium Alloys," in *Review of Progress in Quantitative NDE vol 12*, 1993, pp. 1735–1742.

[20] F. J. Margetan, I. Yalda, R. B. Thompson, and J. Umbach, "Ultrasonic grain noise modeling: recent applications to engine titanium inspections," in *Review of Progress in Quantitative NDE vol 16*, 1997, vol. 16, pp. 1555–1562.

[21] M. V Felice, A. Velichko, P. Wilcox, T. Barden, and T. Dunhill, "Optimization of ultrasonic array inspections using an efficient hybrid model and real crack shapes," *Rev. Prog. Quant. NDE (AIP Conf. Proc. vol 1650)*, pp. 978–986, 2015.

[22] J. H. Rose, "Ultrasonic backscatter from microstructure," in *Review of Progress in Quantitative NDE vol 11*, 1992, pp. 1677–1684.

[23] C. Li, D. Pain, P. D. Wilcox, and B. W. Drinkwater, "Imaging composite material using ultrasonic arrays," *NDT E Int.*, vol. 53, pp. 8–17, Jan. 2013.

[24] M. B. Drozdz, "Efficient Finite Element Modelling of Ultrasound Waves in Elastic Media," *Imp. Coll. London Mech. Eng. PhD Thesis*, 2008.

[25] S. Weyer and A. Fröhlich, "Automatic finite element meshing of planar Voronoi tessellations," *Eng. Fract. Mech.*, vol. 69, no. 8, pp. 945–958, 2002.

[26] P. Huthwaite, "Accelerated finite element elastodynamic simulations using the GPU," *J. Comput. Phys.*, vol. 257, pp. 687–707, Jan. 2014.

[27] S. Chaffaï, V. Roberjot, F. Peyrin, G. Berger, and P. Laugier, "Frequency dependence of ultrasonic backscattering in cancellous bone: Autocorrelation model and experimental results," *J. Acoust. Soc. Am.*, vol. 108, no. 5, p. 2403, Nov. 2000.

[28] A. J. Croxford, P. D. Wilcox, B. W. Drinkwater, and G. Konstantinidis, "Strategies for guided-wave structural health monitoring," *Proc. R. Soc. A Math. Phys. Eng. Sci.*, vol. 463, no. 2087, pp. 2961–2981, 2007.

[29] A. Van Pamel, P. Huthwaite, C. R. Brett, and M. J. S. Lowe, "A finite element model investigation of ultrasonic array performance for inspecting polycrystalline materials," *Rev. Prog. Quant. NDE (AIP Conf. Proc. vol 1650)*, pp. 1007–1014, Mar. 2015.

[30] P. D. Wilcox and A. Velichko, "Efficient frequency-domain finite element modeling of two-dimensional elastodynamic scattering.," *J. Acoust. Soc. Am.*, vol. 127, no. 1, pp. 155–65, 2010.

[31] J. Zhang, B. W. Drinkwater, and P. D. Wilcox, "Defect characterization using an ultrasonic array to measure the scattering coefficient matrix.," *IEEE Trans. Ultrason. Ferroelect. Freq. Control*, vol. 55, no. 10, pp. 2254–65, Oct. 2008.

[32] D. Gabor, "Theory of communication. Part 1: The analysis of information," *J. Inst. Electr. Eng.*, vol. 93, no. 26, pp. 429–441, 1946.

[33] M. Feldman, "Hilbert transform in vibration analysis," *Mech. Syst. Signal Process.*, vol. 25, no. 3, pp.

735–802, Apr. 2011.
[34] A. Ishimaru, *Wave Propagation and Scattering in Random Media*. New York: Academic Press, 1978.

Material Property	Inconel 600
C_{11}	234.6 GPa
C_{12}	145.4 GPa
C_{44}	126.2 GPa
ρ	8260 kg/m^3

Table 1: material properties for Inconel 600 from [14].

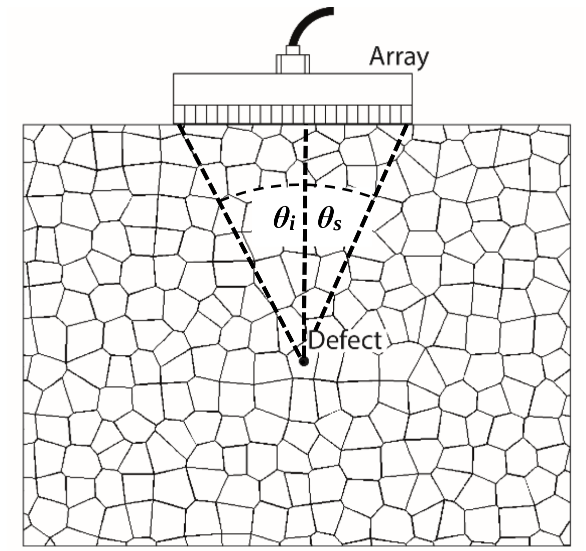

(a)

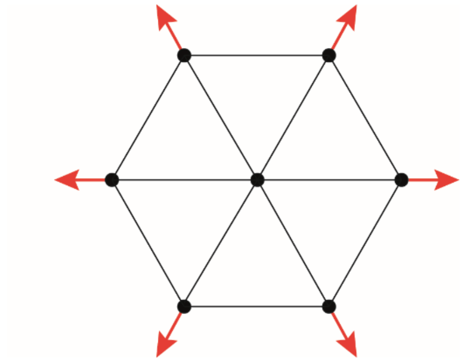

(b)

Figure 1: (a) Schematic of the Finite Element array model layout (not drawn to scale) and (b) schematic of the true point scatterer implementation into FE.

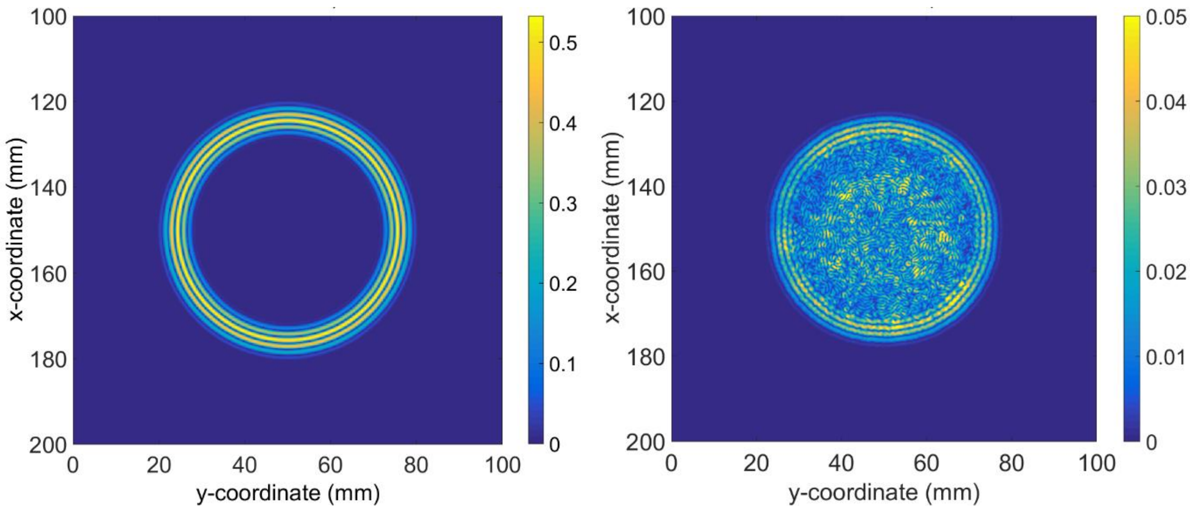

Figure 2: FE illustration of the wave field emanating from a true point source (TPS) propagating after 5μs within (a) isotropic homogenous and (b) polycrystalline material. The colour scale denotes the displacement amplitude at the selected time.

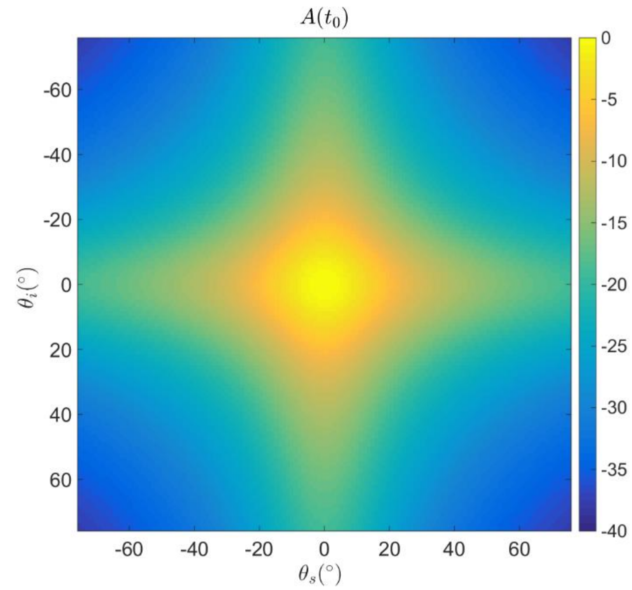

(a)

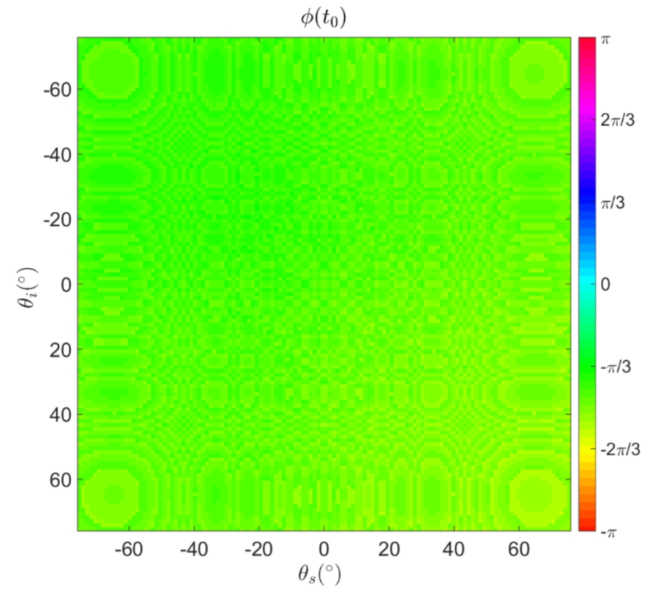

(b)

Figure 3: Scattering matrix for a TPS embedded in isotropic material at a 50mm depth showing (a) amplitude normalised by the peak, and (b) wrapped instantaneous phase shown in radians.

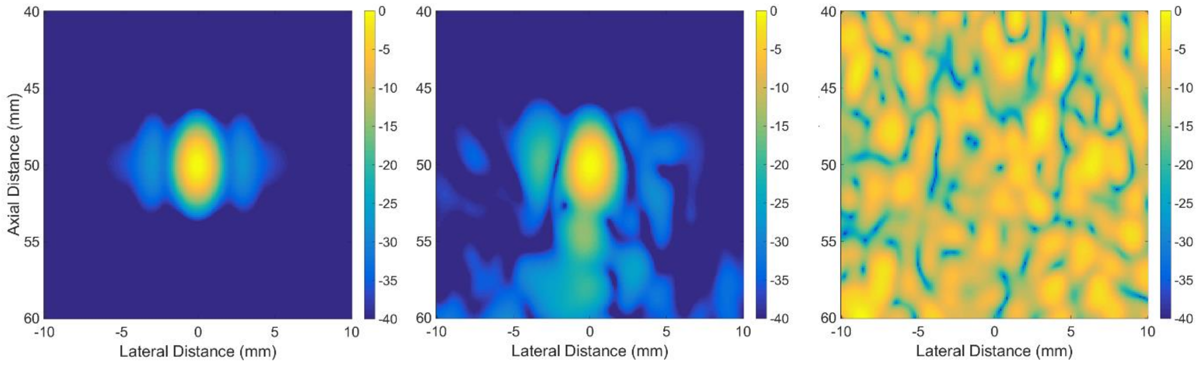

Figure 4: (a) Point Spread Function for an isotropic material (b) aberrated Point Spread Function for a polycrystalline material (c) noise baseline for a polycrystalline material.

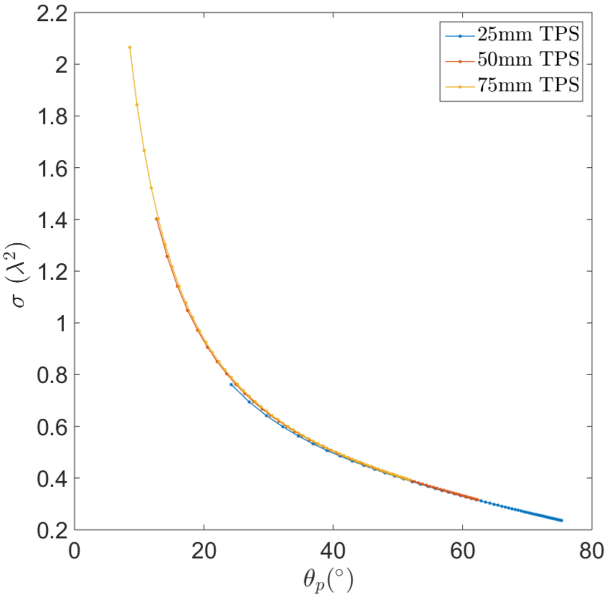

(a)

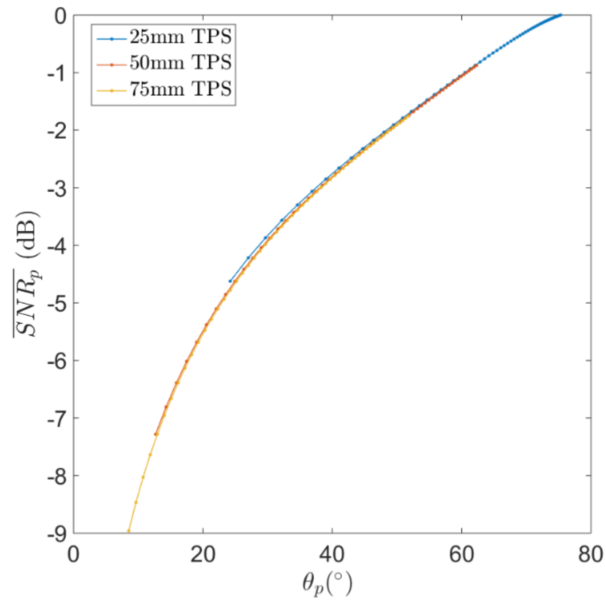

(b)

Figure 5: Simulation results for a true point scatterer embedded within a single scattering medium at 25mm, 50mm, 75mm depth. (a) PSF area versus half aperture angle (b) relative SNR versus half aperture angle.

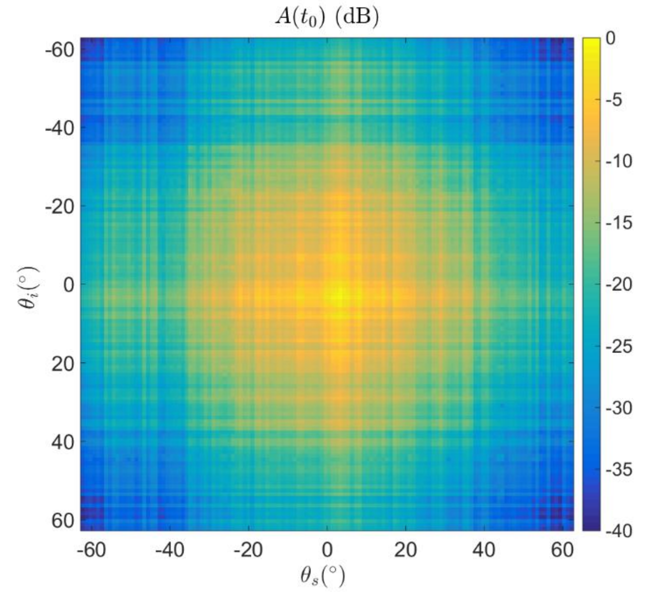

(a)

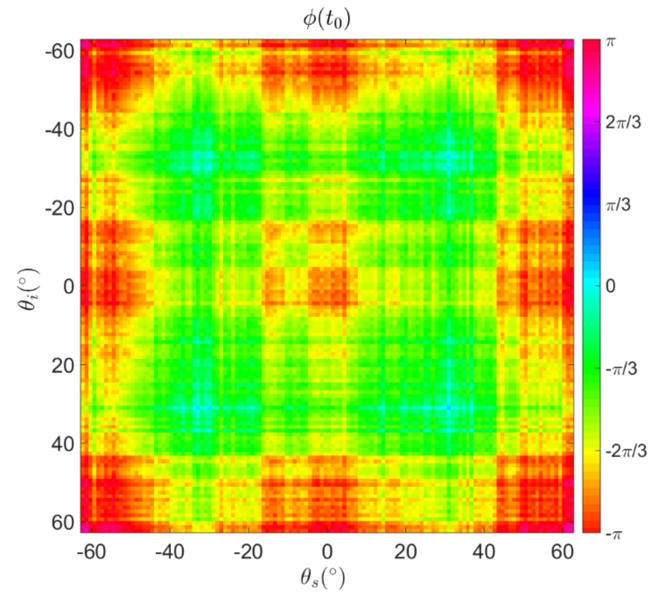

(b)

Figure 6: Scattering matrices for a true point scatterer at 50mm depth in a single realisation of a polycrystalline material, indicating (a) instantaneous amplitude and (b) instantaneous phase against incident and scattered angle.

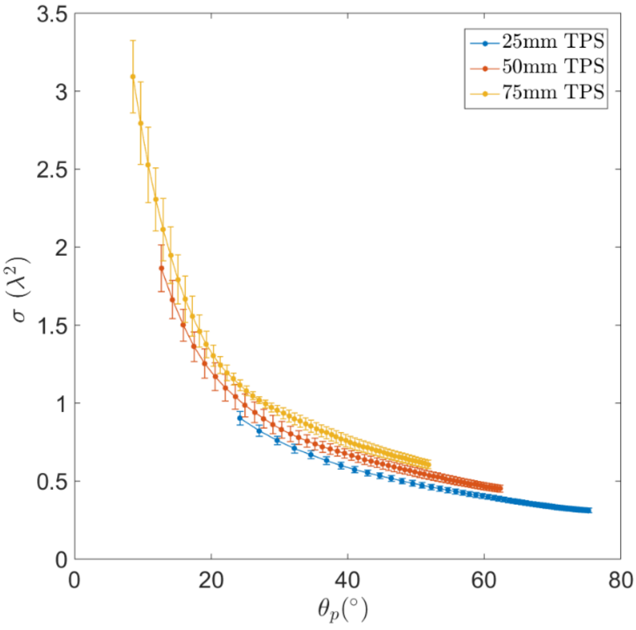

(a)

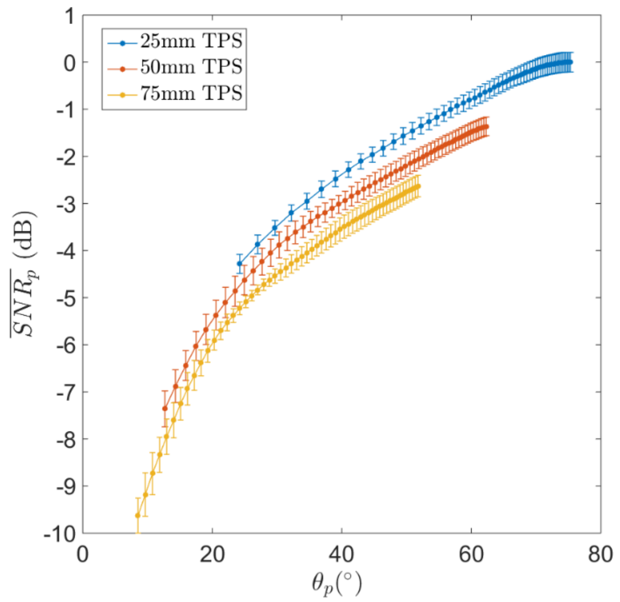

(b)

Figure 7: (a) PSF against half aperture angle for a true point scatterer embedded within a polycrystalline material. (b) mean SNR against half aperture angle calculating under single scattering assumptions. Results obtained by averaging from eight realisations of material with the same grain statistics.

.

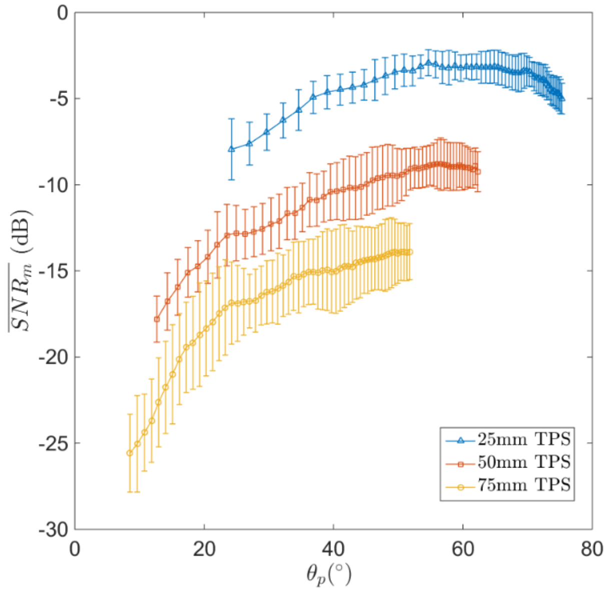

Figure 8: The mean SNR versus half aperture angle for 8 different realisations of a polycrystalline material and for three true point scatterers at 25,50, and 75mm depth.

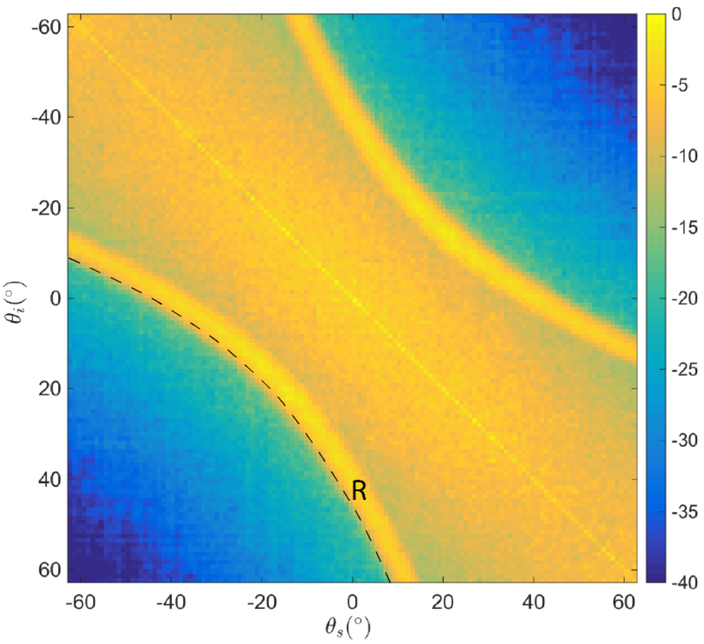

(a)

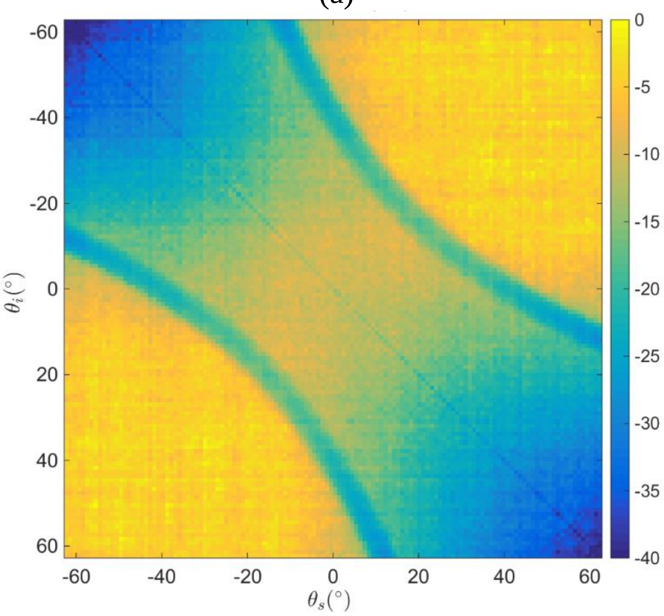

(b)

Figure 9: The (a) RMS noise and (b) mean SNR_m averaged from eight realisations of a polycrystalline material, and calculated as a function of incident and scattered angle. Both figures are normalised to the peak value in the image.

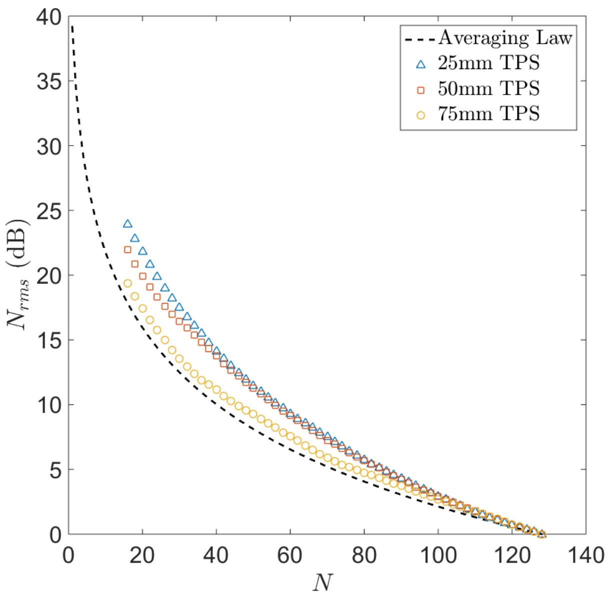

Figure 10: Comparison of the averaging law against the RMS image noise at three different depths, 25mm, 50mm, and 75mm, each from calculated from eight images of backscattering from polycrystalline materials. The results are plotted as a function of the number of array elements *N*.

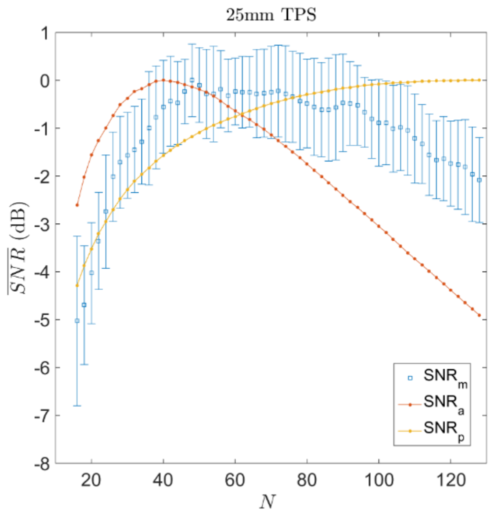

(a)

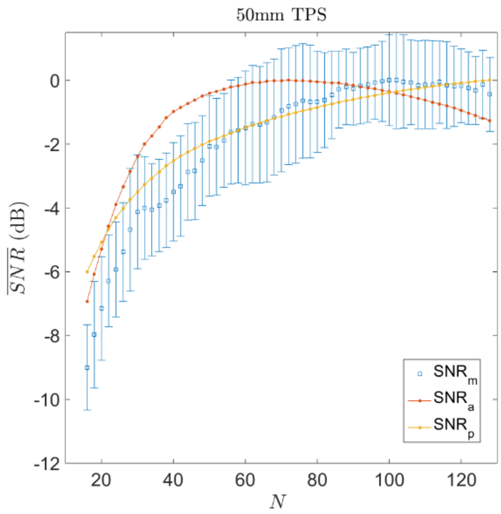

(b)

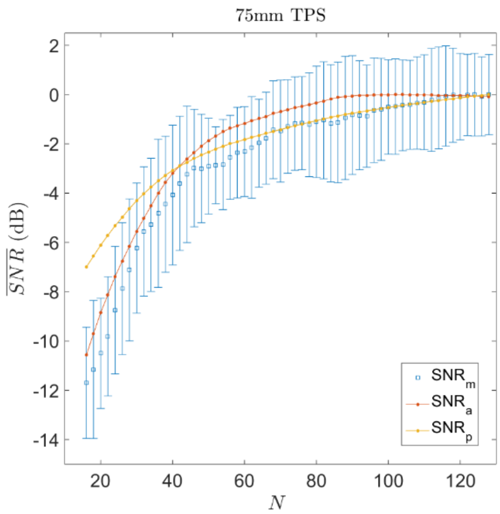

(c)

Figure 11: Comparison of the measured (true) SNR_m with two predicted SNRs: SNR_p which is calculated under single scattering approximations, and a second SNR_a, based on an averaging law. The results are plotted as a function of array element N which varies from 16 to 128, for three true point scatterers embedded at (a) 25mm (b) 50mm and (c) 75mm depth within eight realisations (see error bars) of a polycrystalline, highly scattering medium. Each curve is normalised according to their maximum.